Low-cost High-Speed Photogrammetry for Measuring Dynamic Flow Deposits

Tzu-Yin Kasha Chen [1], Chi-Yao Hung [2], Michael Scheiber [1,3], Kimberly Hill [1,4]

[1]St. Anthony Falls Laboratory, University of Minnesota, 2 Third Ave SE, Minneapolis, 55414, Minnesota, USA
[2]Department of Soil and Water Conservation, National Chung Hsing University, No. 145, Xingda Rd., Taichung 402, Taiwan
[3]Institute of Mountain Risk Engineering, University of Natural Resources and Life Sciences, Vienna Gregor-Mendel-Straße 33, Vienna 1180, Austria
[4]Department of Civil, Environmental, and Geo-Engineering, University of Minnesota, 500 Pillsbury Dr SE, Minneapolis 55455, Minnesota, USA

Key Points:

- Cost-effective, advanced photogrammetry for precise measurement in particle-fluid flow experiments using WiFi cameras.
- Standout for cost-effectiveness and robust design; external synchronization with flash lamps enables capture of dynamic flow events.
- Applied successfully in debris flow experiment; tracks growth, evolution, links local flow to channel avulsion events.

Corresponding author: Chi-Yao Hung, cyhung@nchu.edu.tw

Abstract

We introduce a novel, cost-effective photogrammetry-based method designed for measuring rapidly evolving three-dimensional surface topography in particle-fluid flow experiments. This method offers high-resolution results over a considerable surface area, enabling the capture of dynamic flow events with temporal granularity limited only by removable memory card capacity. Multiple WiFi-enabled security cameras, meticulously calibrated with precision-measured reference points on calibration boards, are employed in this methodology. External synchronization, facilitated by strategically-positioned flash lamps, allows calibration among cameras without additional precise tools. Validating our method through an alluvial fan experiment showcases its efficacy in tracking the growth and evolution of experimental debris flows, particularly in capturing the dynamic evolution of debris flow deposits on a growing alluvial fan. This example illustrates the method's ability to link local flow, evolution, and deposition to multiple channel avulsion events, highlighting its success in capturing distinct slope and height dependencies associated with these phenomena. Overall, our method transcends conventional measurement approaches, providing a significant advancement in capturing the intricacies of rapidly evolving three-dimensional surface topography in particle-fluid flow experiments. Its cost-effectiveness and robustness make it a valuable tool for diverse, dynamic scenarios, presenting a promising solution for experimental laboratory-scale landscape studies.

Plain Language Summary

We've developed a new and affordable way to measure the changing shape of surfaces in experiments where particles interact with fluids. Our method uses multiple WiFi-enabled security cameras that are carefully set up and synchronized using flash lamps. This allows us to capture high-resolution images of dynamic events in the flow, with the only limitation being the memory card capacity. We tested our method in an experiment simulating debris flows on a growing fan of sediment. The results showed that our approach is effective in tracking the growth and changes in the flow, especially in capturing how debris settles on the fan. This method goes beyond traditional measurement techniques, offering a significant improvement in understanding the complex shapes that emerge in particle-fluid flow experiments. Its affordability and reliability make it a valuable tool for studying various dynamic scenarios in experimental landscape studies.

1 Introduction to the Applications: Large Scale Multi-phase Flows and Their Deposits

Geological particle-fluid flows – including lahars, snow avalanches, debris flows, and fluvially-transported sediment – typically form large-scale geomorphological structures upon deposit such as river deltas and alluvial fans (e.g., in Figure 1). Understanding the evolving flow/deposit interactions would help inform a better understanding of ancient sedimentary deposits as well as modern surficial hazards; depositional structures carry signatures of the complex flows under which they were formed. Material details such as grain / liquid concentrations, presence of clay as well as width of grain size distribution influence the flow dynamics and, in turn, channelization, channel avulsion rate, and other details. However, the co-evolution of flow content, flow dynamics, and deposit morphology is difficult to predict or even measure in part because of the dynamically-evolving flow details, such as local rheology and frictional and pressure forces along their boundary. Additionally, even though the flows carry solid materials (particles) that are similar if not identical to those in the beds over which they traverse, the dynamics that control variation between relatively simple erosional and depositional periods of interactions with the bed are only minimally understood. The combined effects often give rise to complex channelization patterns on the surface over which the flows travel (Figure 1a-b).

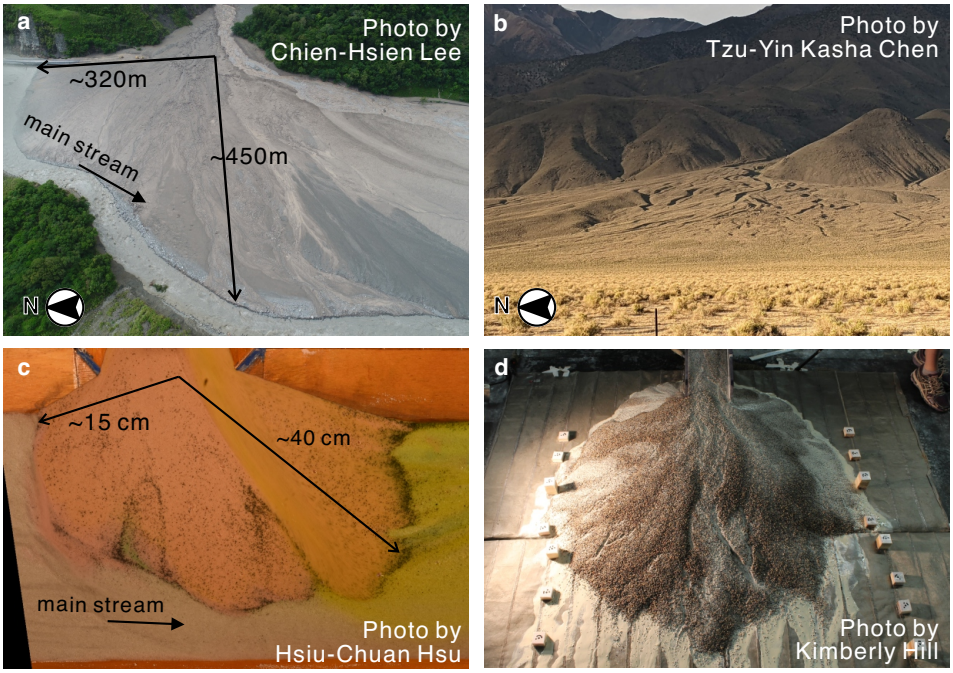

Figure 1. Debris flow fans with channels. (a) Yu-Shui Fan, Laonong River, Southern Taiwan. (b) Straight Fan, Owens Valley, California, USA. (c) Experimental debris flow deposit (Hsu, 2018). (d) Experimental fan deposit (Chen et al., 2022).

Historically, our understanding of these natural systems has been shaped by field research incorporated into numerical models (Dietrich & Krautblatter, 2019; Dietrich, 2020), along with the use of massive hillslope experiments (Iverson et al., 2010) and large laboratory experiments (Hsu, 2018). Field data is limited by the hazards associated with the large-scale flows, and detailed data acquisition in the field and in the experimental flows is limited in terms of interactions along the base of the flow that, indeed, dictate the flow/channel interactions. Large-scale experiments are also expensive and limited (Iverson et al., 2010). To supplement the data available at larger scales, much progress has been made in using laboratory experiments much more modest in their size. Because of the possible broad scope under which geomorphologically-significant dynamics can be explored in these smaller experiments, this work is focused on new developments related to increasing the details that can be extracted.

While at first glance these exhibit what one might call "unreasonable effectiveness" at mimicking geomorphic phenomenology at field scale (Paola et al., 2009), they have provided immeasurable insight into previously less-understood natural problems. A few examples include studies of dam and dike breaches (Rifai et al., 2016, 2020); avulsion behaviors of rivers on floodplains and fans (Bryant et al., 1995), including cohesive effects (Martin et al., 2009) on fans; and debris flows (Kaitna et al., 2016) and the fans onto which they deposit (de Haas et al., 2016a, 2018; Chen et al., 2022).

To achieve a full accounting of interactions between flows and surfaces onto which they deposit, many efforts have been devoted to imaging surficial details and their evolution under repeated flow events. Some examples include airborne Lidar in field (Mallet & Bretar, 2009; Webb et al., 2018) and laser profilometry in laboratory (Huang et al., 2010; Hung & Capart, 2013; Rifai et al., 2017, 2020), which both provide extremely high-resolution and precise measurements though are mostly appropriate for relatively stationary surfaces. Another option is photogrammetry, which extracts three-dimensional

information from multiple overlapping two-dimensional images and is typically a more affordable method to construct topographic details both in field (Lane, 2000; Yanites et al., 2006; Westoby et al., 2012; Yang et al., 2018; Eltner et al., 2018; Filhol et al., 2019) and in the laboratory (Morgan et al., 2017; Balaguer-Puig et al., 2017; Piton et al., 2018; Polvi, 2021; Leenman & Eaton, 2021). Lidar, the most expensive of these options, uses a coherent laser beam to capture surface details and thus can more effectively image ground through leaves and other vegetation, whereas photogrammetry uses a wide range of frequencies in the visible light spectrum, which makes it more difficult to reject details associated with trees / plants. In experiments in which plants are not used, this is not a restriction.

In recent years, some studies have used photogrammetry to capture slowly evolving surfaces in the laboratory. For example, Guo et al. (2016); Jiang et al. (2020); Balaguer-Puig et al. (2017) studied soil erosion and rill development at flume scales using the topographic data from photogrammetry. In this case, the dynamics were sufficiently slow that temporal resolutions greater than 1-minute time-steps were sufficient. Leenman and Eaton (2021) studied fluvial deposits on alluvial fans with 1-minute temporal resolution, also sufficient for the dynamics they studied. They employed nine digital single-lens reflex cameras for high spatial resolutions. Alternatively, Piton et al. (2018) investigated open channel flows and utilized photogrammetry to record experimental fluvial topography, employing flow stoppage and drainage before each photogrammetry time step. However, this method is limited to situations where the topography remains unaffected by the drainage process, and the dynamic of the channel evolution is not influenced by the flow stoppage.

In many laboratory experiments, surfaces evolve more quickly, and such repeated drainage steps are not possible. At first glance, it appears the use of photogrammetry is not possible in discerning frequently changing details. Further, because of the requirement of multiple overlapping photos for each DEM data, for high-speed results, one would need multiple cameras for high-resolution topography on a relatively large deposit ($\sim$ 1 m $\times$ 1 m) (de Haas et al., 2016b; Chen et al., 2022), not widely affordable. Possibly for these reasons, dynamic topographic measurement methods are not well-established for rapidly evolving surfaces, like fans built from debris flows. Indeed the specific photogrammetry technique adaptable for the laboratory – structure-from-motion (Ullman, 1979) – appears less well-known in the community for experimental adaptation (Morgan et al., 2017).

In this context, we introduce a relatively inexpensive system for measuring topography at high-frequency acquisition rates for system sizes limited only by the number of relatively inexpensive cameras used. Towards this, we introduce structure-from-motion techniques using data acquired by relatively inexpensive "security" cameras in conjunction with distortion-resolving software. To illustrate the effectiveness of this method, we present preliminary analyses of avulsion events on a 1 m^2 alluvial fan as it builds and develops over 15 minutes. We discuss strengths of this technique as well as limitations in its current form. We conclude by presenting opportunities for expanding the analysis beyond its current usefulness.

2 Low-cost High-speed Structure from Motion (SfM) Photogrammetry for Large Laboratory Experiments

The foundation of our new low-cost real-time topography acquisition and analysis system consists of two primary components: (1) the physical image acquisition system comprised primarily of multiple low-cost security cameras and calibrated reference points, and (2) the Structure from Motion (SfM) image analysis technique that converts overlapping 2-D images to a 3-D deposit surface. In addition to these primary components, we instituted several additional components to enhance the semi-automated struc-

tural analysis of experimental surfaces as they evolve over time. In the following subsections, we present the details of these primary and supporting components.

2.1 Experimental Image Acquisition System and Supporting Elements

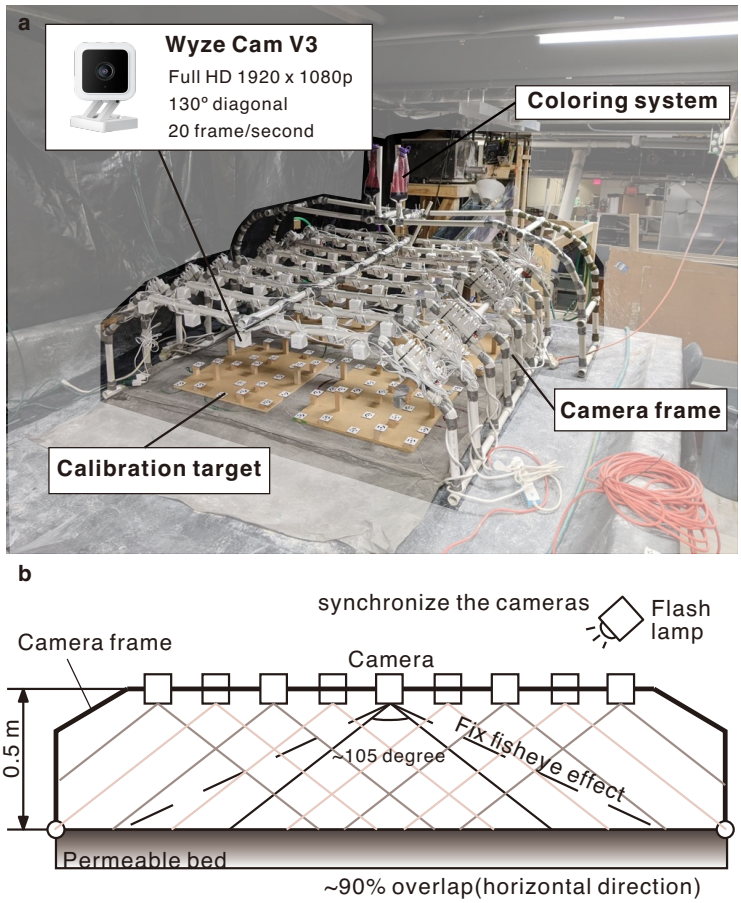

Figure 2. Photogrammetry and supporting systems. (a) Photograph in the laboratory, (b) sketch from downstream view.

2.1.1 Photogrammetry Acquisition System

To quantitatively record the evolution of the morphology of our deposit, our photogrammetry measurement system consists of (1) an image acquisition frame and (2) spatially distributed reference points (Figure 2).

For the photogrammetry technique to work, we need to have a number of points in space that can be distinguished from one another by the SfM software and whose location is known to be the same or better precision required of the DEM data. Further, the points must be distributed spatially in all three dimensions in such a way as to encompass the expected range of surface data locations. Finally, the reference points must be arranged in such a way that, during the camera calibration period, each camera can capture at least three distinct reference points.

For the spatial calibration reference system, we built four calibration boards (Figure 2). Each calibration board contained 25 12-bit circular reference point patterns (Franzini

et al., 2016) that can be automatically distinguished by the imaging software. The locations of the reference points vary vertically and horizontally across the range of the deposit. Before each experiment, we place the calibration boards in the deposition region in such a way as to encompass the expected distribution of the surface of our deposit (Figure 2). We then use a laser profilometry (laser scan) system at the St. Anthony Falls Laboratory to obtain the three-dimensional coordinates of all reference points (100 reference points). After laser scanning the reference points, we install the cameras for that experiment.

The image acquisition system requirements for the Structure from Motion (SfM) technique include sufficient numbers of cameras (of sufficient resolution) so that all locations on the surface of interest are captured by at least 5, and preferably, up to 10 cameras (Fonstad et al., 2013). For our deposits which typically grow to 1.5×1.5 m^2 in plan view, we use approximately 70 cameras we mounted to a homemade frame (made of PVC tubes) above the evolving deposit. We use Wyze Cam V3 cameras (security cameras roughly priced at USD 30 per camera), which provide a fair image resolution (1080 x 1920 pixels), a wide field of view (130° diagonal, albeit with the fish-eye effect we discuss shortly), and a frame rate of 20 fps. We mounted the cameras on the PVC tube frame in a staggered array at a distance of approximately 50 cm from the base (Figure 2). This provides an 89% overlap in the neighboring camera image area in the lateral direction and a 59-76% overlap in the basin slope direction, resulting in more than 8-camera overlap for most of the viewing region.

In addition to the details we address during the set-up of the basic image acquisition system, several special issues arise because of the temporal coordination we require and also specific conditions associated with particle-fluid deposits in the geomorphological applications of interest to us. We present our methods for overcoming these issues in the following section.

2.1.2 Additional Experimental Components for SfM of Experimental Particle-Fluid Deposits

The use of relatively low-priced security cameras limits the ability to temporally calibrate the picture acquisition from all of the cameras. The security cameras we used do, in fact, have a built-in time synchronization function, but it does not satisfy our needs given the (sub-second) speed at which our experimental deposit surfaces evolve. Therefore, to calibrate our cameras, we used reference events at the beginning and end of our experiments. In particular, we used a Nikon SB900 flashlamp we set with a duration similar to the frame rate of the cameras. More specifically, the brightest part of each flash lasts for $1/20s$ and the brightness rises and falls over a slightly longer time (though less than 1/4 s). We flashed the lamp multiple (five) times shortly before the beginning of the flow initiation of our experiment and we repeated this after the flow was complete to verify the stability of the calibration. After the experiment was complete, we input the recordings of these flashes into a homemade code to assign an initial timestep common for all cameras. Essentially, we use the rising limb of the brightness of each flash recorded in the movie to synchronize the cameras as we describe in section 2.2 (along with our other computational image analysis techniques).

Another difficulty in the application of SfM techniques for our systems involves resolving relatively flat mono-colored regions (e.g., Ullman, 1979). If a region of the surface of interest is particularly flat and mono-colored, images acquired from different cameras may not be sufficiently distinct for SfM algorithms to resolve the topography of that region. To provide distinct patterns on the fan surface that the photogrammetry software can use to guide the surface-building algorithms, throughout the duration of the experiment we add different streams of food coloring to incoming flows to the apex of our deposit. Towards this, we constructed a food coloring frame on which to mount four

food coloring feeding bags over the camera frame (Figure 2). We turned on the outflow of the feeding bags and adjusted the outflow location throughout the experiments to ensure the coverage of the food coloring over the fan surface.

Another issue that can negatively affect the image quality during the image acquisition stage is the reflectivity of that surface. For example, this occurs in our experiments when and where our surface is highly reflective due to excessive moisture and the local fluid flow. In these cases, the camera images differ partly because of the difference in reflection from their different vantage points, differences unrelated to the surface texture. To diminish this we eliminate point sources of bright lights during the experiment and use multiple diffuse light sources.

2.1.3 Experimental Acquisition System Set-up and Procedures

Once we prepare these different systems for image acquisition, we perform the following steps to measure our reference points, then capture images of the reference point towards calibrating our cameras, and finally record the evolving surface over the duration of the experiment. We place our four calibration boards on the surface of the soon-to-grow deposit. We measure the calibration points with the laser scanner as described above. Then, we move the frame with mounted cameras over the reference point calibration boards and initiate the cameras. That is, we connect all security cameras to a monitoring device (cell phone) through WiFi. After initiation, each security camera continuously records videos to a micro SD card installed within the camera. With the help of the monitoring device, we adjust the positions and orientations of each camera to ensure that each camera views at least 10 reference points (Fonstad et al., 2013). Once the cameras are oriented in a satisfactory way, we allow them to record images of the calibration boards for a few minutes, we then remove the calibration boards without changing camera positions, and the cameras are ready to record.

2.2 Image Analysis

Once we have completed the experiment, we upload all videos to a computer with Structure from Motion software and other image processing techniques we detail shortly.

2.2.1 Structure from Motion (SfM) Image Analysis Technique

Structure from Motion (SfM) is a relatively well-known image analysis technique that creates 3-D models of object surfaces from 2-D images. We use the commercial Agisoft software package to process our images in this way. Originally, it was a technique developed literally to use multiple images taken of a surface from a moving camera (the "motion" part of the nomenclature) to reconstruct the 3-D details (structure) of the surface (Ullman, 1979). In fact, it is not the motion of the camera that matters, rather, images must be taken from multiple vantage points. Since the images must be acquired at an effectively minimal time difference (in the time scale of an evolving surface), it is more effective in a fast-changing surface to use multiple cameras as we do in our approach. Then we can use the SfM technique to convert multiple 2-D images taken at the same time to create 3-D models of our surface for as many timesteps as we have data. The problem of reconstructing a 3-D surface from multiple 2-D images has been the focus of a large body of research in the field of "computer vision", starting from the seminal paper by Longuet-Higgins (1981). More modern approaches are reviewed by Özyeşil et al. (2017).

Computational algorithms extract 3-D surface features from multiple 2-D images following several steps. They first extract features (such as corners or edges) from images and match them across multiple images. Once these features are matched, the relative camera position and orientation for each image can be computed. These can then be used to reconstruct the 3-D structure of the scene. One of the advantages of SfM is

that it can be done using a relatively inexpensive setup, such as a consumer-grade camera (or cameras). We note, however, that the accuracy and quality of the 3-D models produced depend on factors such as the number and quality of the input images, the camera calibration, and the feature-matching algorithms' accuracy.

While the above describes the minimal considerations for such an SfM system, there are some common issues in the experiments we designed this technique for that need to be considered in the overall design for the technique to be effective. We describe some of the details we encountered along with their solutions presently.

2.2.2 Additional Components for Image Processing

Several image processing steps are necessary to ensure high-quality photogrammetry results. We describe the steps here and provide the Matlab code we use in the Open Research section.

To start the processing, we first have to calibrate the timeline of the videos from each camera with one another. This is not as straightforward as it seems; while the security cameras all take pictures at a rate of 1/20 Hz over the 0.05 s duration, some are capturing images while others are between images and effectively have their shutters closed. In other words, each flash is recorded with various levels in the different cameras. First, our code calculates the brightness of each image from the beginning of the movie recorded by each camera. Then our code calculates the change of brightness from each image to the next in a subset of the images recorded near the same time as the brightest image. It uses a threshold to find the biggest positive gradients in this time period. Because of the nature of the flashlamp and the cameras, it finds five rising pairs. The fifth rising pair indicates the time step of each camera capturing the flashlight performed at the beginning of the experiment $t = 0$.

For all images we want to be processed, i.e., used to create DEM data, we note that all camera lenses create optical distortion, and the security cameras with wide fields of view have an especially strong fish-eye effect (Figure 3a). However, using images without distortion to build three-dimensional topographies is ideal. To correct the perspective in the images, we took a set of images of a checkerboard and used the algorithms provided by Scaramuzza et al. (2006) to correct the optical distortions for the image data recorded by each camera (Figure 3b). We then trim each corrected image down to 559 x 1359 pixels with a reduced field of view (110° diagonal, 105.8° horizontal, and 57.1° vertical) to keep the full rectangular image without blanks (Figure 3c). We then use these corrected images for all the steps that follow.

After following these steps, we are ready to process the images in the commercial SfM software, Agisoft Metashape and to build digital elevation models (DEM) and orthogonal photos (orthophoto). To do so, we first import the images of the reference points (described above in section 2.1) and the coordinates of the reference points to the software. The software detects each image's 12-bit circular reference points and calibrates the camera coordinates (positions and rotation angles). We then use a Python script to trigger Agisoft Metashape to build the DEMs and orthophotos for multiple time steps by batch processing. By using an i5-9500 Intel processor, it takes around 3 minutes to complete the process for each time step.

To determine the times at which we want high temporal resolution data for our experiments (described in the next section) we find it useful to first go through this process (correct image distortion, and build and export the data) at a frequency of 1/s for the whole duration of the experiment. Based on the results, we can choose a specific part of the experiment to repeat this process at a higher frequency for a shorter time interval, up to a maximum frequency of 20 per second (DEM's of ~ 1 mm^2 spatial resolution and orthophotos of ~ 1 mm per pixel resolution).

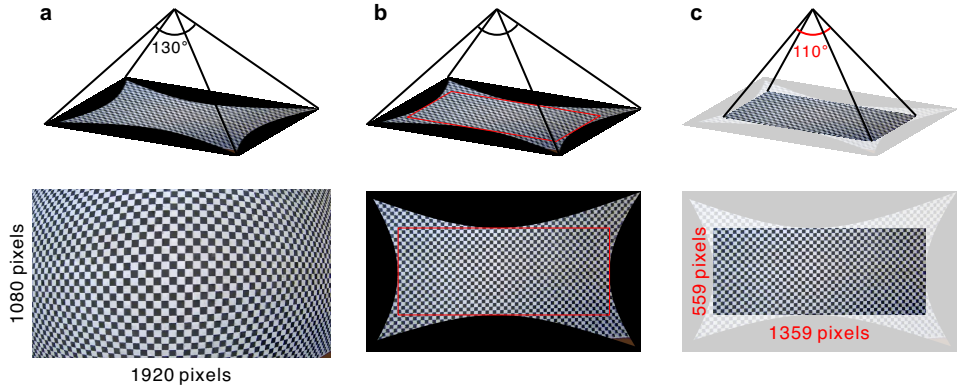

Figure 3. Image fish-eye distortion correction. (a) Image from the security camera with a fish-eye effect, (b) undistorted image with blanks, and (c) trimmed full rectangular image without blanks.

3 Experimental Fan Set-up

As a testbed for these measurements, we used an experimental setup comprised primarily of a flume-basin system (Figure 4a) nearly the same as that described by Chen et al. (2022). Specifically, a narrow inclined rectangular channel (2m-long × 0.2m-wide, slope = 0.3) conveys sediment-liquid mixtures to a wide basin (3m-wide × 5m-long, slope = 0.118). For these experiments, we installed a permeable bed layer (1.8m × 1.8m) on the basin surface made of rubber drainage tiles and covered by a #200 mesh screen sheet.

The use of photogrammetry in the way we describe herein does not limit the material choice except for certain details described in the previous section. We designed our sediment-fluid mixture for this paper based on a subset of experiments described in Chen et al. (2022) for which conditions were ideal for relatively simple channelization and channel evolution. These mixtures consisted of 50 w% angular sand (specific gravity of 2.65), 4 w% clay (Kaolinite with specific gravity of 2.65), 45.996 w% water, and 0.004 w% Polydiallyldimethylammonium chloride (PDADMAC), a flocculent.

To ensure a constant mixture throughout the experiment, we premix the liquid mixture (clay/water/flocculent) in a drum and pump it up into a head tank which discharges (at a constant rate) into a funnel mixer operating slightly above the upstream end of the channel. Simultaneously, we use a sediment feeder to input the sand at a constant rate into the same funnel mixer. The entire mixture leaves the funnel well-mixed into the upstream end of the flume and flows to the channel/basin transition (See Chen et al. (2022) for details). The boundary conditions at the channel-to-basin transition loosely resemble those of a transition from canyon-lands to a wide-open depositional area for debris flows. At the transition, there is a sudden decrease in slope and effective width, slowing the progression of the mixture further downslope. The bed permeability allows the liquid to leave the flow from its base and intensifies the reduction of speed at which the remaining mixture travels downslope where it subsequently deposits. As the sand settles in the deposit, it captures some of the clay and the rest drains through the permeable bed. This leaves a soft, moist clay-sand deposit.

As described by Chen et al. (2022), during the first few minutes of these experiments, the experimental debris flows build what becomes the base of the deposit whose surficial features we aim to study. After ten minutes, after sufficient fan growth, the channelization behavior becomes apparently statistically consistent; the details appear closer to a representative of the field cases we aim to understand, and the channelizations and

avulsions appear to regularize. Since it is this latter behavior that we designed the SfM set-up to measure, we report on deposition details during this 10 to 15-minute period of the experiment. The final deposit is approximately cone-shaped and has a plan area of ≈ 1 m^2 (Figure 4b).

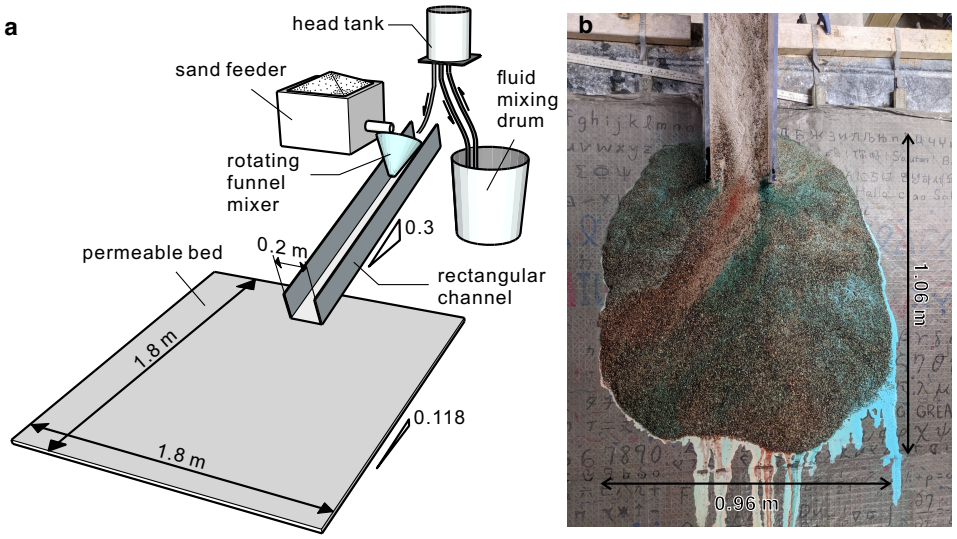

Figure 4. Debris flow fan experiment. (a) Experiment set-up, (b) photograph of the experimental fan resulting from continuous 15-minute releases with (sand: clay: water) = (50: 4: 46) by weight.

4 Results: Simultaneous Flow and Topography Measurements

4.1 Snapshots of Channels and Topography

To illustrate some of the basic details captured by the imaging system, we present data from six time steps of the debris fan experiment in Figure 5. The first and third columns contain the orthophotos (derived from Agisoft-calculated height data) for the times noted at the bottom of each. To the right of each orthophoto, the second and fourth columns contain slope maps with height contours associated with the same times.

The orthophotos contextualize the more quantitative data in the topography data. The coloration in these images originates from the natural sediment colors and the dies. There is no relationship between color and topography in these images; rather they help us follow the evolution of the flow paths, particularly when they are combined sequentially to create a movie (see supplementary video).

The topography plots in columns two and four of Figure 5 have three sets of information distinguished by color scheme: (1) slope data (indicated in the turbo rainbow colorbar); (2) elevation data (indicated with thin black contour lines, provided in 5mm height increments), and (3) black pixels that indicate missing data as we discuss shortly. For the elevation data in these images, we first use Agisoft to calculate the height data to a resolution of 2 mm $\times$ 2 mm. Then we smooth these data using a 10 mm diameter moving average filter to remove roughness associated with individual sand particles. We then calculate the slope data from the smoothed height data.

While strictly speaking, the black pixels contain no height data, we find we can use them in conjunction with the orthophotos to help us discern the active channel(s) from

the rest of the surface. While there could be many reasons for missing data points from SfM processing, in our case we identify two primary regions of concentrated points of missing DEM data. The solid black rectangle at the top of each image corresponds to a region within the base of the channel for which we cannot obtain local DEM data because of local shading issues. Most of the rest of the black pixels correspond to localized surface fluid. For relatively isolated missing pixel data, we conjecture reflection from surface fluid inhibits height calculations. Regions containing high densities of black pixels in the height data correspond to the channelized flow, verifiable in the movie of joined orthophotos (see supplemental video).

Considering all of this, we revisit the snapshots in Figure 5 for insight into some channel dynamics from the corresponding time interval during our experiment. Figures 5a-b indicate that, at ≈ 622 seconds into the experiment, two active channels coexisted on the surface, as indicated with arrows in Figure 5b. Additional analysis described below indicates that one was an established longer-lasting channel (arrow 1) and the other was a smaller narrow more short-lived channel (arrow 2). From Figures 5c-f we can see that during the next ≈ 10 s, the primary channel gradually migrated toward the center of the fan while the secondary channel disappeared. At $t \approx 634$ s (Figures 5i-j), the primary channel avulsed, relatively suddenly, to the left of the center of the fan. From the topography maps of the previous time steps, we can see this avulsion was spatially associated with a narrow region – a "gully" – with higher slopes (green color) than the neighboring areas. That is, after the quick avulsion, the new location of the channel corresponded to the location of this gully. With additional analysis, we present in Section 4.2, we found that the primary flow followed the channel in the gully a bit longer until it avulsed again.

These snapshots provide valuable information about the location and evolution of channels and associated slope maps. In these snapshots, we see evidence of both slow and fast channel avulsion and associated channel changes. Nevertheless, the snapshots in and of themselves are limited in how they give us insights on the timescales of the avulsions. Even more valuable information comes from our ability to combine the relative high-speed DEM data from this technique into a form that represents a more continuous view of the evolution of the morphology. In the next section, we provide an example of the type of data that can be discerned from a more continuous presentation of the time evolution.

4.2 Spatio-Temporal Plots of Surface Features

We can combine high temporal resolution data into spatio-temporal plots to elucidate the time dependence(s) of the co-evolution of surface topography and channel avulsions. In Figure 6 we illustrate the additional insight such plots can provide in our demonstration fan case.

We illustrate how this might be used with a focused analysis of evolution in the central region of the fan (Figure 6) rather than the fan apex or toe region, where changing boundary conditions influence flow details. Towards this, we use DEM data (such as those in Figure 5) that is restricted to the region of the surface that is both more than 300mm from the fan apex and whose height above the permeable base is more than 30mm. We illustrate the region of interest in the top row of Figure 6. We then average slope data in this region of each figure in the radial direction. We use the polar coordinate system for which the origin $r = O$ is located at the fixed apex of the fan; r increases outward from the apex in the plan view of the orthophoto, and $\phi = 0$ set along the center line of the fan and increases counterclockwise.

We can plot these together in a spatio-temporal plot. We plot the radially-averaged fan slope from this central region as a function of both ϕ and t in Figures 6d-e. The data are plotted in Figure 6d based on resolutions of $\Delta\phi = 0.05$ rad and $1/20s$ for the same

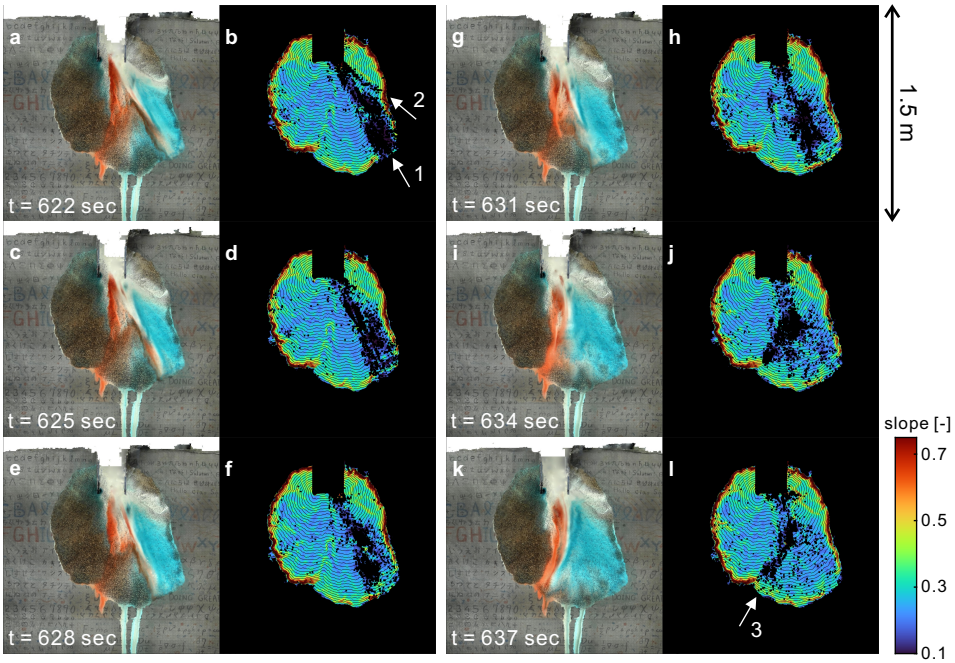

Figure 5. Two series of fan data from photos taken 3 sec apart at approximately 10.5 minutes from the start of the discharge as noted in the first and third columns. Columns 1 and 3: orthophotos constructed from the data at times (in sec) indicated in bottom left corners. Colors are from dye injections during the experiments, not indicative of any particular features. Columns 2 and 4: Topography maps for the same six time steps. Coloration indicates local slopes via a color bar at the bottom right. Regularly-spaced black curved line: elevation contours with 5mm elevation spacing. The black bar near the center top is indicative of the bottom of the channel. Other black regions on the interior of the fan indicate regions for which no DEM data was obtained at that time step, likely due to surface moisture and reflectance. White arrows indicate outlets of two channels.

time represented by the panels in Figure 5, that is, between 600 and 660 seconds. For Figure 6e, we plot these for one frame per second for the time frame between 600 and 900 seconds.

Superposed on the slope map, we plot the location of the flowing regions in greyscale. Since we cannot precisely identify the flows by the DEM data, we use the information from the distorted pixel regions (black in Figure 5) to approximate these data. We do so by a modified smoothing algorithm. For each pixel, we consider the number of distorted pixels within a circular region of radius 20 mm (approximately 316 pixels). If more than 75% of those nearby pixels are distorted in the DEM we plot that central pixel as one with surface flows (pink in Figures 6a-c). For each time step, we count the number of pixels in each solid angle and plot it based on the greyscale defined at the right of Figure 6e. Many other choices for this spatially-averaged spatio-temporal plot; for this example, we consider this framework and then we discuss effects of alternative settings briefly in Section 5.2.

For ease in interpretation of these images, we draw the reader's attention to a few details. At approximately 620 s (the time of the first panels in both Figure 5 and 6) two channels are apparent in the spatio-temporal plot, highlighted with white arrows in Figure 5 and black in the spatio-temporal plots in Figures 6d-e. Channel 2 (at approximately

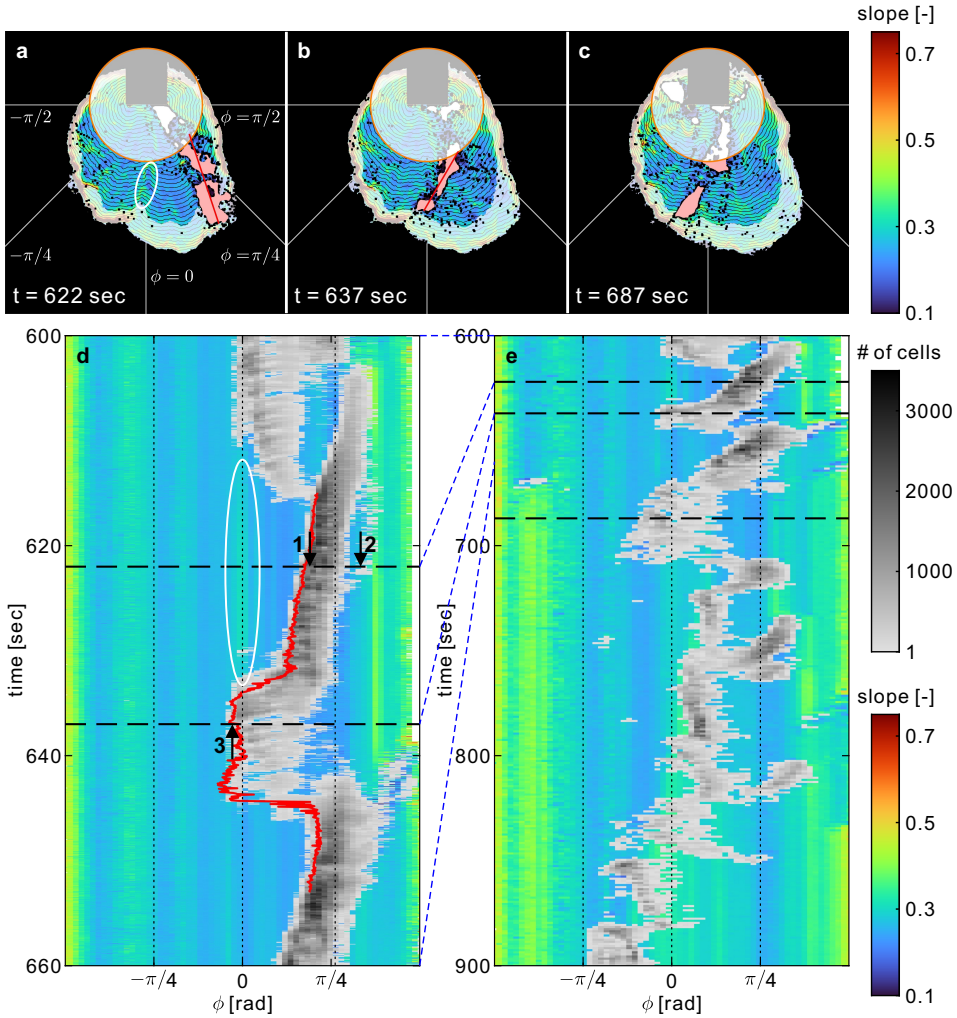

Figure 6. Avulsion analysis. (a)-(c) Illustration of the regions of analysis. Colored region: regions of slope analysis that are not adjacent to the fan apex and toe. Orange line: the ellipse that defines the region adjacent to the fan apex. Pink region: captured channels that are not adjacent to the fan apex. Red line: regression line for the pink region. (d)-(e) Spatio-temporal plot of the measures of slope and channel location. Thick dashed lines in (d): $t = 622$ and 637 seconds. Thin dash line in (d): the angular coordinates of the end of the regression line. Thick dash in (e): $t = 622$, 637, and 687 seconds.

5/36 π) is a minor channel and, from the spatio-temporal plot, appears to be a remnant from an earlier flow and disappears shortly after $t = 622$ s. Channel 1 is a more significant channel and appears to be migrating at a roughly steady pace toward the fan center. At approximately 635 s, we see evidence of a much faster avulsion, just crossing the center line of the fan in Figure 6b. When we consider the slope map information along with the channel information in this case, we see that the new location is one associated with a higher slope prior to this avulsion (white ellipse in Figures 6a and d). When the channel avulses away from this location at approximately 645 s, we can see that the channel left behind a region of lower slope (blue rather than green at $\phi \approx 0$). These details provide evidence of the mechanics behind channel avulsion.

We now turn our attention to the longer-time plot in Figure 6e. In this plot, we can see many similar sequences, particularly between angles of $\phi = -\pi/4$ to $+\pi/4$ indicating this is a predominant sequencing: a higher slope appears to motivate channel avulsion to the region, and, subsequently, the channel deposits downstream leading to a lower slope. In addition to the occurrence at $\phi \approx 0$ between $\approx$ 635 s to 645 s mentioned above, we see evidence of a similar event at $\phi \approx \pi/4$ between $t \approx$ 730 s and 760s. There is a wealth of information that can be mined in these plots for further modeling of these systems. For example, there are also times channel avulsion events increase the local slope (e.g., at $\approx \phi = -3\pi/8$ when $t \approx 670$ s.) We can use these maps to get data for the rate at which channels traverse azimuthally for the slow avulsions. For example, we may calculate an *effective slope* of the avulsion path on the spatio-temporal plots to get the rate of azimuthal movement vs time.

These provide a context for interpreting avulsion events. They can be somewhat limited by the choices of spatial averaging that was performed. However, with further analysis of different resolutions we can derive many additional types of information to build a more robust set of models for avulsions on fans.

5 Discussion

5.1 Data Resolution and Comparison to Data from Laser Profilometry for Particular Time Steps

In this section, we aim to compare the quality of the DEMs generated by our SfM method with those generated by laser profilometry, while also discussing the crucial role of the number of cameras used in constructing the DEM. Figure 7a displays the topography map of the final deposit produced by the SfM method, revealing some noise on the permeable bed due to reflections, where patterns are challenging to identify. The red-scale slope illustrates the fan surface morphology distinctly. Figure 7b presents the topography map obtained by laser scanning after a period for drainage after the experiment, covering part of the fan due to conflicts in the basin and laser scan system configurations. The laser scan, with a 0.5 mm per pixel resolution, effectively captures the permeable bed without noise and depicts a rugged fan surface with higher local slopes attributed to sediment particles.

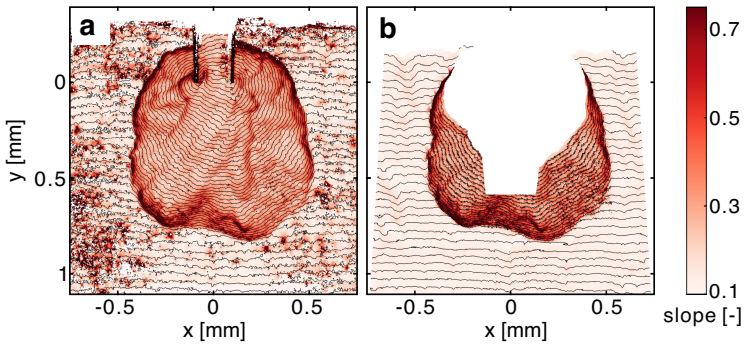

Figure 7. Results for the final fan deposit. (a) topography map generated from the photogrammetry method. Red scale presents the surface slope. Black line: elevation contours with 5mm elevation spacing. (b) Topography map generated from the laser scan method. Symbolic as panel a.

Qualitatively, the SfM method results mirror the characteristics and shape of laser profilometry. In quantity comparison, we subtract the DEM captured by SfM from the

laser scan-based DEM, showcasing differences in Figure 8c, with the red line representing the outer boundary of the fan. SfM result provides elevation data for 93.8 % of the region with laser scan elevation data and 99.7 % within the fan boundary. Notably, both methods yield closely aligned results in most regions on the fan surface, with larger vertical differences occurring mainly on the permeable bed outside the fan boundary and along the fan toe with steep slopes. Figure 8d presents the distribution of vertical differences, showing mean absolute values of 1.37 mm for the entire basin and 1.34 mm for the fan region.

These results demonstrate that within our experimental setup, our method constructs topography with comparable high accuracy to laser profilometry, and it achieves this in less than one second per image acquisition, offering continuous measurement opportunities with the same precision.

The determination of the camera count emerges as a pivotal factor influencing DEM precision. To understand this impact, we systematically manipulated the number of cameras, examining resulting variations in spatial coverage and computing height disparities when contrasted with laser scan data. This comparative analysis spans the entire basin, focusing on the fan region.

To compute camera coverage, we leveraged calibrated camera coordinates and orientations in the SfM software, projecting the reduced field of view of each camera onto the inclined planar surface aligned with the permeable bed. Figure 8b illustrates non-uniform camera view times in the domain, with most regions where fan material was deposited viewed by at least 8 cameras and some by up to 28 cameras. The average camera view times in the fan region were 18.9.

Reducing the camera count to 52 cameras lowered the average views in the fan region to 13.9 (ranging from 6 to 22). Under these conditions, the photogrammetry method showed increased disparities from laser scan data, particularly near the fan toe and on the permeable bed, with more regions lacking photogrammetry data (11.1 % in areas with laser scan elevation data and 0.52 % within the fan boundary with laser scan data). The distribution of vertical differences, presented in Figure 8h, showed mean absolute values of 1.46 mm for the entire basin and 1.41 mm for the fan region.

Further reducing the camera count to 38 (as shown in Figure 8i) resulted in an average of 9.4 camera views in the fan region (ranging from 3 to 15). This condition accentuated disparities between photogrammetry and laser scan data, with more regions lacking photogrammetry data (18.7 % in areas with laser scan elevation data and 4.8 % within the fan boundary with laser scan data). The distribution of vertical differences in Figure 8l showed mean absolute values of 2.11 mm for the entire basin and 2.48 mm for the fan region distribution.

As shown in Figure 8, our findings indicate a substantial decrease in accuracy and an increase in missing data as the number of cameras is reduced. The straightforward recommendation for improved measurements is to employ more cameras, assuming that the camera quality adequately resolves details on the target. It is crucial to note that this suggestion is contingent upon the assumption that the camera resolution is sufficiently high to capture intricate details on the target. In instances where the camera resolution is inadequate for this purpose, increasing the camera count will not enhance the precision of the DEMs.

5.2 Discussion of Channel Identification

This study demonstrates the potential application of high-resolution DEMs in investigating the avulsion process on debris fans. However, identifying the channel presents challenges, introducing uncertainties in understanding this complex process. As the con-

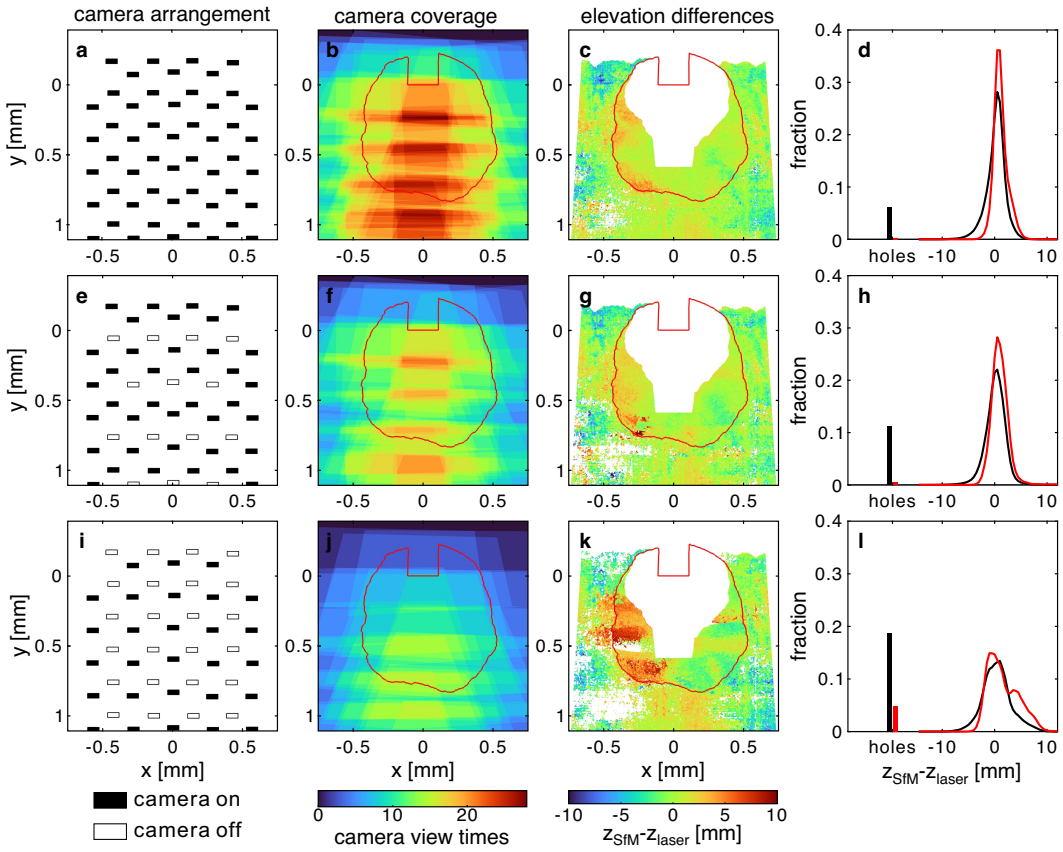

Figure 8. Effect of reducing camera numbers. Column 1: camera arrangements. Solid block: positions of cameras selected to use. Open block: positions of cameras not selected to use. Column 2: camera view times on the plane aligned with the permeable bed. Red line: fan boundary. Column 3: elevation differences between the data measured by the SfM method and the laser scan. Column 4: distribution of the elevation differences between the two methods. Black: data in the basin with laser scan data; red: data in the fan region where there are laser scan data. Row 1: 70 cameras, Row 2: 52 cameras, Row 3: 38 cameras.

struction of DEMs on water surfaces is unfeasible, an alternative approach involves utilizing information from nearby pixels to identify the channel location. This is accomplished by implementing a modified smoothing algorithm with two key parameters: a radius denoted as r and a threshold ratio denoted as p applied to the topography. For each pixel, the algorithm considers the number of distorted pixels within a circular region of radius r. If more than the ratio p of nearby pixels are distorted, the central pixel is flagged as exhibiting surface flows (depicted in pink in Figures 6a-c). The chosen parameter values ($r = 20$ mm and $p = 0.75$) in this study specifically target the avulsion of medium and large channels. The results of the algorithm are illustrated by varying r between 15, 20, and 25 mm and p between 0.5, 0.75, and 0.95 in Figure 9, accompanied by a thorough discussion of the effects of these two parameters.

Examining the impact of increasing the ratio p in Figure 9, channels identified by the algorithm exhibit a narrowing trend from the left to the right column. Notably, the offset between the identified channels (depicted in pink) and the distorted pixel regions' boundaries (depicted in black) becomes more pronounced.

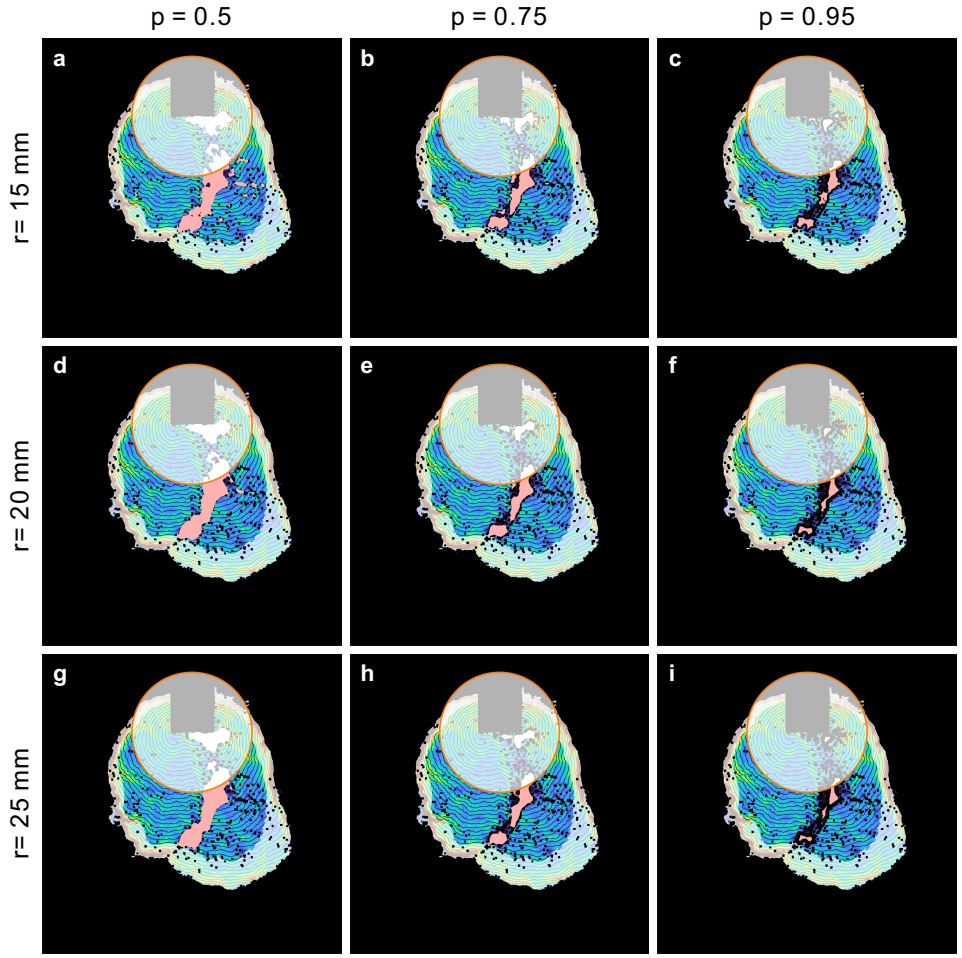

Figure 9. Channel capture. Colored region: regions of slope analysis that are not adjacent to the fan apex and toe. Orange line: the ellipse that defines the region adjacent to the fan apex. Pink region: captured channels that are not adjacent to the fan apex.

Further analysis focuses on the effects of increasing the radius r in Figure 9. Moving from the top to the bottom row, the influence of the surroundings intensifies. Small channels are notably diminished (illustrated by the scattered channels in panels a, d, and g). Medium channels exhibit reduced width (observed in the primary channels in panels b, c, e, f, h, and i). Conversely, large channels demonstrate less susceptibility to these changes (illustrated in the primary channels in panels a, d, and g). In summary, adjusting r and p can enhance the capture of small channels, while larger values of r and p are more effective in focusing on larger channels.

5.3 Addressing Limitations and other Future Directions

In the course of this investigation, we have presented an innovative and cost-effective methodology for the construction of high-resolution Digital Elevation Models (DEMs) across both temporal and spatial dimensions. This methodology has provided a robust foundation for a comprehensive exploration of the intricate dynamics involved in the channel avulsion process. However, it is incumbent upon us to acknowledge and address certain inherent limitations in our approach.

Primarily, the current reliance on a flash lamp for camera synchronization introduces a temporal precision constraint, tethered to the frame rate of the camera and the duration of the flash. This constraint poses a limitation on the applicability of our method to subjects characterized by a movement whose critical details are faster than the frame rate of the camera. The part of the post-processing that links a particular frame from each camera to all cameras has the limitation of likely being slightly out of synch over the time step of 1 / (frame rate). Furthermore, such cameras have frame rates approximately as specified, so when the initial post-flash images are linked from all cameras at the beginning of the run, they progressively become out of step, which may become serious for longer run requirements. At present, this can be addressed by periodic manual resynchronization at specific times during data processing, but for a longer run this can become tedious. To surmount this constraint and enhance temporal precision, we advocate for the exploration and implementation of new synchronization methods. A judicious selection of synchronization techniques can potentially broaden the scope of our methodology, making it adaptable to a wider array of dynamic phenomena.

Furthermore, as alluded to earlier in this discourse, the presence of water reflection poses additional problems for analysis, potentially compromising measurement accuracy. This issue is particularly pronounced in experiments with higher water content, where the introduction of noise to the DEM becomes a pertinent concern. Mitigating this challenge, particularly for experiments with pervasively high water content, will require strategic intervention. We suggest the application of polarizers attached to all camera lenses, which may provide a practical solution to minimize reflections from the water surface. We plan to incorporate this optical tool to enhance the precision and reliability of our measurements, ensuring the fidelity of the DEM even in conditions with heightened water content.

Leveraging the methodology we have devised, we find its versatility in measuring diverse experimental scenarios marked by swift alterations in topography. The significance of this capability becomes pronounced in processes demanding continuous measurement, where any interruptions in experimentation can yield substantial discrepancies. Notable instances encompass the assessment of dam breach processes (Rifai et al., 2016, 2020), the investigation of river avulsion phenomena on floodplains (Bryant et al., 1995), and the scrutiny of the evolving fan deposition in debris flows occurring at the confluence of trunk rivers and tributaries (Hsu, 2018). In these contexts, the continuous and uninterrupted application of our methodology proves invaluable, enabling a comprehensive understanding of the intricate and dynamic topographical transformations. By extending our methodological application to these diverse scenarios, we pave the way for nuanced insights into the temporal and spatial dynamics of these natural processes.

In the future, we plan to expand the versatility of our methodology beyond topography evolution by incorporating Particle Tracking Velocimetry (PTV) into the image analysis. By concurrently capturing topographical changes and particle locations from various camera angles, our approach enables the effective tracking of surface particles. This integration facilitates the construction of a detailed and nuanced depth-averaged 3-D velocity field, offering insights into the dynamic behaviors of particles within the studied environment. In essence, our methodology provides a multifaceted toolkit for nuanced experimentation and analysis, transcending the boundaries of traditional measurement techniques. As we continue to refine and expand our approach, we anticipate its broader application across a spectrum of dynamic processes, contributing to the advancement of scientific understanding and exploration.

6 Summary

This paper introduces an innovative, cost-effective, and high-speed photogrammetry method tailored for capturing a diverse array of geomorphological processes, encom-

passing sediment transport, deposition, and topographic evolution, specifically emphasizing rapidly unfolding phenomena. The method's core components include many affordable cameras, spatial calibration reference points, and flashlight signals for precise temporal calibration. Utilizing data from these devices with commercial photogrammetry software, such as Agisoft Metashape, facilitates the creation of high-resolution spatial and temporal datasets. The study is centered on the application of this method in laboratory debris flow fans, showcasing its capacity to comprehensively capture the morphodynamic development, including orthogonal images and DEMs at 1/20-second intervals for ~ 1 m^2 debris flow fans constructed over 15 minutes. Remarkably, the method adeptly records channels and their avulsion processes, capturing both sudden and gradual avulsions. The dynamic topography data obtained enables an in-depth investigation into the mechanisms governing these processes, offering valuable insights into the co-evolution of fan morphology and channels. While the experimental results illustrate the potential to explore correlations between avulsion processes and topographic changes, it is essential to acknowledge the paper's focus on a single experiment. Moreover, the paper underscores the method's inspirational potential, particularly its accessibility due to its low cost, making it a viable tool for a broader audience engaged in physics-based understanding and hazard modeling through readily available datasets.

7 Open Research

The Matlab codes for camera synchronization, raw videos of all cameras for the experiment, coordinates of the reference points, and example topography data of the experiment (DEM in 1 fps for 600-900 seconds) are available at Chen et al. (2024), https://doi.org/10.5281/zenodo.10421490.

The Python script for triggering the batch processing in Agisoft Metashape used in this paper is built according to Metashape Python Reference (Agisoft LLC, 2019).

Acknowledgments

The researchers express their gratitude for the kind and valuable aid provided by the research team at St. Anthony Falls Laboratory. This project received financial support from the Young Scholar Fellowship Program of the National Science and Technology Council (NSTC) in Taiwan, grant number 111-2636-M-005-001, and the National Science Foundation (NSF), grant numbers EAR-1451957 and EAR-2127476.

References

Agisoft LLC. (2019). *Metashape python reference, release 1.6.0* [Book]. Agisoft LLC. Retrieved from `https://www.agisoft.com/pdf/metashape_python_api_1_6_0.pdf` (last access: 14 February 2022)

Balaguer-Puig, M., Ángel Marqués-Mateu, Lerma, J. L., & Ibáñez-Asensio, S. (2017). Estimation of small-scale soil erosion in laboratory experiments with structure from motion photogrammetry. *Geomorphology*, *295*, 285-296. doi: https://doi.org/10.1016/j.geomorph.2017.04.035

Bryant, M., Falk, P., & Paola, C. (1995). Experimental study of avulsion frequency and rate of deposition. *Geology*, *23*(4), 365–368.

Chen, T.-Y. K., Hung, C.-Y., Mullenbach, J., & Hill, K. (2022). Influence of fine particle content in debris flows on alluvial fan morphology. *Scientific Reports*, *12*(1), 21730.

Chen, T.-Y. K., Hung, C.-Y., Scheiber, M., & Hill, K. (2024). *Model codes and data for "Low-cost High-Speed Photogrammetry for Measuring Dynamic Flow Deposits".* Zenodo. doi: 10.5281/zenodo.10421490

de Haas, T., Densmore, A., Stoffel, M., Suwa, H., Imaizumi, F., Ballesteros-Cánovas,

J., & Wasklewicz, T. (2018). Avulsions and the spatio-temporal evolution of debris-flow fans. *Earth-Science Reviews*, *177*, 53–75.

de Haas, T., van den Berg, W., Braat, L., & Kleinhans, M. G. (2016a). Autogenic avulsion, channelization and backfilling dynamics of debris-flow fans. *Sedimentology*, *63*(6), 1596–1619.

de Haas, T., van den Berg, W., Braat, L., & Kleinhans, M. G. (2016b). Autogenic avulsion, channelization and backfilling dynamics of debris-flow fans. *Sedimentology*, *63*(6), 1596-1619. doi: https://doi.org/10.1111/sed.12275

Dietrich, A. (2020). *Debris flows in the northern alps–activity, erosivity and anticipated volumes* (Unpublished doctoral dissertation). Technische Universität München.

Dietrich, A., & Krautblatter, M. (2019). Deciphering controls for debris-flow erosion derived from a lidar-recorded extreme event and a calibrated numerical model (roßbichelbach, germany). *Earth Surface Processes and Landforms*, *44*(6), 1346–1361.

Eltner, A., Elias, M., Sardemann, H., & Spieler, D. (2018). Automatic image-based water stage measurement for long-term observations in ungauged catchments. *Water Resources Research*, *54*(12), 10,362-10,371. doi: https://doi.org/10.1029/2018WR023913

Filhol, S., Perret, A., Girod, L., Sutter, G., Schuler, T. V., & Burkhart, J. F. (2019). Time-lapse photogrammetry of distributed snow depth during snowmelt. *Water Resources Research*, *55*(9), 7916-7926. doi: https://doi.org/10.1029/2018WR024530

Fonstad, M. A., Dietrich, J. T., Courville, B. C., Jensen, J. L., & Carbonneau, P. E. (2013). Topographic structure from motion: a new development in photogrammetric measurement. *Earth Surface Processes and Landforms*, *38*(4), 421-430. doi: https://doi.org/10.1002/esp.3366

Franzini, F., Soares-Frazão, S., & Capart, H. (2016). Measurement of the free-surface elevation in a steady flow in complex topography using photogrammetry. In *River flow* (pp. 581–587).

Guo, M., Shi, H., Zhao, J., Liu, P., Welbourne, D., & Lin, Q. (2016). Digital close range photogrammetry for the study of rill development at flume scale. *CATENA*, *143*, 265-274. doi: https://doi.org/10.1016/j.catena.2016.03.036

Hsu, H.-C. (2018). *Debris flow fan morphodynamics at a confluence in a mobile bed channel* (Master Thesis). National Chung Hsing University.

Huang, M. Y. F., Huang, A. Y. L., & Capart, H. (2010). Joint mapping of bed elevation and flow depth in microscale morphodynamics experiments. *Experiments in Fluids*, *49*, 1121–1134.

Hung, C.-Y., & Capart, H. (2013). Rotating laser scan method to measure the transient free-surface topography of small-scale debris flows. *Experiments in fluids*, *54*, 1–17.

Iverson, R. M., Logan, M., LaHusen, R. G., & Berti, M. (2010). The perfect debris flow? aggregated results from 28 large-scale experiments. *Journal of Geophysical Research: Earth Surface*, *115*(F3).

Jiang, Y., Shi, H., Wen, Z., Guo, M., Zhao, J., Cao, X., ... Zheng, C. (2020). The dynamic process of slope rill erosion analyzed with a digital close range photogrammetry observation system under laboratory conditions. *Geomorphology*, *350*, 106893. doi: https://doi.org/10.1016/j.geomorph.2019.106893

Kaitna, R., Palucis, M. C., Yohannes, B., Hill, K. M., & Dietrich, W. E. (2016). Effects of coarse grain size distribution and fine particle content on pore fluid pressure and shear behavior in experimental debris flows. *Journal of Geophysical Research: Earth Surface*, *121*(2), 415–441.

Lane, S. N. (2000). The measurement of river channel morphology using digital photogrammetry. *The Photogrammetric Record*, *16*(96), 937-961. doi: https://doi.org/10.1111/0031-868X.00159

Leenman, A., & Eaton, B. (2021). Mechanisms for avulsion on alluvial fans: Insights from high-frequency topographic data. *Earth Surface Processes and Landforms*, *46*(6), 1111–1127.

Longuet-Higgins, H. C. (1981). A computer algorithm for reconstructing a scene from two projections. *Nature*, *293*(5828), 133–135.

Mallet, C., & Bretar, F. (2009). Full-waveform topographic lidar: State-of-the-art. *ISPRS Journal of Photogrammetry and Remote Sensing*, *64*(1), 1-16. doi: https://doi.org/10.1016/j.isprsjprs.2008.09.007

Martin, J., Sheets, B., Paola, C., & Hoyal, D. (2009). Influence of steady base-level rise on channel mobility, shoreline migration, and scaling properties of a cohesive experimental delta. *Journal of Geophysical Research: Earth Surface*, *114*(F3).

Morgan, J. A., Brogan, D. J., & Nelson, P. A. (2017). Application of structure-from-motion photogrammetry in laboratory flumes. *Geomorphology*, *276*, 125-143. doi: https://doi.org/10.1016/j.geomorph.2016.10.021

Özyeşil, O., Voroninski, V., Basri, R., & Singer, A. (2017). A survey of structure from motion*. *Acta Numerica*, *26*, 305–364.

Paola, C., Straub, K., Mohrig, D., & Reinhardt, L. (2009). The "unreasonable effectiveness" of stratigraphic and geomorphic experiments. *Earth-Science Reviews*, *97*(1-4), 1–43.

Piton, G., Recking, A., Le Coz, J., Bellot, H., Hauet, A., & Jodeau, M. (2018). Reconstructing depth-averaged open-channel flows using image velocimetry and photogrammetry. *Water Resources Research*, *54*(6), 4164-4179. doi: https://doi.org/10.1029/2017WR021314

Polvi, L. E. (2021). Morphodynamics of boulder-bed semi-alluvial streams in northern fennoscandia: A flume experiment to determine sediment self-organization. *Water Resources Research*, *57*(3), e2020WR028859. doi: https://doi.org/10.1029/2020WR028859

Rifai, I., Erpicum, S., Archambeau, P., Violeau, D., Pirotton, M., Abderrezzak, K. E. K., & Dewals, B. (2016). Monitoring topography of laboratory fluvial dike models subjected to breaching based on a laser profilometry technique. In *River sedimentation* (pp. 380–386). CRC Press.

Rifai, I., Erpicum, S., Archambeau, P., Violeau, D., Pirotton, M., El Kadi Abderrezzak, K., & Dewals, B. (2017). Overtopping induced failure of noncohesive, homogeneous fluvial dikes. *Water Resources Research*, *53*(4), 3373-3386. doi: https://doi.org/10.1002/2016WR020053

Rifai, I., Schmitz, V., Erpicum, S., Archambeau, P., Violeau, D., Pirotton, M., ... El Kadi Abderrezzak, K. (2020). Continuous monitoring of fluvial dike breaching by a laser profilometry technique. *Water Resources Research*, *56*(10), e2019WR026941.

Scaramuzza, D., Martinelli, A., & Siegwart, R. (2006). A toolbox for easily calibrating omnidirectional cameras. In *2006 ieee/rsj international conference on intelligent robots and systems* (p. 5695-5701). doi: 10.1109/IROS.2006.282372

Ullman, S. (1979). The interpretation of structure from motion. *Proceedings of the Royal Society of London. Series B. Biological Sciences*, *203*(1153), 405–426.

Webb, R. W., Jennings, K. S., Fend, M., & Molotch, N. P. (2018). Combining ground-penetrating radar with terrestrial lidar scanning to estimate the spatial distribution of liquid water content in seasonal snowpacks. *Water Resources Research*, *54*(12), 10,339-10,349. doi: https://doi.org/10.1029/2018WR022680

Westoby, M., Brasington, J., Glasser, N., Hambrey, M., & Reynolds, J. (2012). 'structure-from-motion' photogrammetry: A low-cost, effective tool for geoscience applications. *Geomorphology*, *179*, 300-314. doi: https://doi.org/10.1016/j.geomorph.2012.08.021

Yang, C.-H., Tsai, M.-H., Kang, S.-C., & Hung, C.-Y. (2018). Uav path plan-

769 ning method for digital terrain model reconstruction – a debris fan example.
770 *Automation in Construction*, *93*, 214-230. doi: https://doi.org/10.1016/
771 j.autcon.2018.05.024
772 Yanites, B. J., Webb, R. H., Griffiths, P. G., & Magirl, C. S. (2006). Debris flow de-
773 position and reworking by the colorado river in grand canyon, arizona. *Water*
774 *Resources Research*, *42*(11). doi: https://doi.org/10.1029/2005WR004847